High Step-Up Current-Fed Diode-Clamped Resonant Converter for Overloaded Fuel-Cell Vehicles

Ji-Ho Choi, *Graduate Student Member, IEEE*, Muhammad Mubeen Khan, Cheol-Hwan Kim, and Minsung Kim, *Senior Member, IEEE*

***Abstract*—We propose a high step-up current-fed diode-clamped resonant converter for overloaded fuel-cell vehicles. The electric motor is able to demand short-time peak torque during sudden acceleration phase or long-time excessive torque when the fuel-cell vehicles are overloaded. Then, the conventional converter suffers from a high current spike at the secondary-side switches. The proposed converter incorporates diode-clamped cell on the secondary side, and therefore does not have the high current spike, but retains the benefits of the conventional converter such as high step-up function, ripple-free characteristic, and soft switching capability. When the output power is over its maximum nominal value, the secondary-side switches are switched OFF with complete zero-voltage-switching (ZVS) and the secondary-side diodes are OFF with zero-current-switching (ZCS). As a result, the proposed converter exhibits high efficiency and long-term operation under the nominal power and even at peak power. Furthermore, we have analyzed voltage gain, ZVS/ZCS region, and current/voltage stress on the active power components when the output power is over its maximum nominal value, which is different from those when the output power is in its nominal range. The theoretical analysis of the proposed converter is presented, then validated using a laboratory-built prototype.**

***Index Terms*—Diode clamping, high step up converter, overloaded vehicles, ripple free, soft switching.**

I. Introduction

THE number of vehicles powered by fuel-cell sources continues to increase to improve the air quality in the cities while reducing the oil dependency in the transportation sector. Fuel-cells have relatively low output voltage compared to the voltage of the dc-bus in the vehicles in which they are used. A dc/dc converter is used to convert this low output voltage of fuel-cells to a constant high voltage; an inverter is followed to convert high voltage into ac voltage compatible with motors. The electric motor itself can demand short-time peak torque during sudden acceleration phase or long-time excessive torque when the fuel-cell vehicles are overloaded. These problems would cause high transient current stress on the power conversion stage. Furthermore, the high-frequency input-current ripple must be low to extend the life-span of the fuel-cell source [1]. Hence, high step-up dc–dc converter that can operate reliably over the maximum nominal output power ($\geq$1 kW) and with low input-current ripple must be used (see Fig. 1) [2], [3].

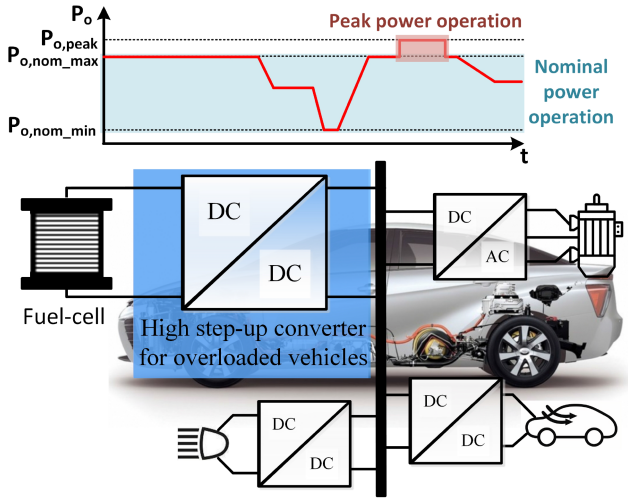

Fig. 1. High step-up DC/DC converter used in electrical systems of fuel-cell vehicles that operates within nominal power range (0.1 kW $\leq P_o \leq$ 1 kW) and at peak power. P_{o,nom_max} is the maximum nominal output power. P_{o,nom_min} is the minimum nominal output power. $P_{o,peak}$ is the peak output power.

Single current-fed topologies are extensively adopted for high step-up applications. Well-developed soft-switching topologies such as SEPIC [4], boost half bridge [5], quasi Z-source [6], [7], [8], coupled inductor and voltage multiplier [9], [10], [11], and switched capacitor-inductor [13], [14], [15] are selected for single current-fed dc/dc converters. The merits of these converters are small amount of high-frequency input current ripple and inherent step-up function. However, single power-transfer path cannot reduce the input current ripple further. Besides, high input current concentrates on the main switch, which leads to high conduction loss. Consequently, the power conversion efficiencies of these converters are low at the peak power level.

Double current-fed structure can decrease the high-frequency input current ripple further and alleviate the current stress on the switching devices because the input current is splitted into multiphase currents. Double current-fed converters were introduced in [16] and [17], but the primary-side switches and

Manuscript received 25 August 2022; revised 18 December 2022 and 31 March 2023; accepted 18 April 2023. Date of publication 24 April 2023; date of current version 21 June 2023. This work was supported in part by the National Research Foundation of Korea (http://dx.doi.org/10.13039/501100003725) grant funded by the Korea government (MSIT) under Grant RS-2023-00210590, and in part by Korea Electric Power Corporation under Grant R22XO02-26. Recommended for publication by Associate Editor Jin Wang. *(Corresponding author: Minsung Kim.)*

The authors are with the Division of Electronics and Electrical Engineering, Dongguk University, Seoul 04620, South Korea (e-mail: jjho@dgu.ac.kr; mubeen2526@dgu.ac.kr; hapydumdum@naver.com; mkim@dgu.ac.kr).

Color versions of one or more figures in this article are available at https://doi.org/10.1109/TPEL.2023.3269626.

Digital Object Identifier 10.1109/TPEL.2023.3269626

the secondary-side diodes are OFF with hard switching. To ensure zero-current-switching (ZCS) turn-OFF of the primary-side switches and secondary-side diodes, the use of auxiliary active clamp circuit [18], [19], [20], snubberless clamping method [21], and resonant pulse technique [22] has been proposed. Nevertheless, these converters still have input-current ripple. To eliminate the ripple, a double current-fed converter with secondary-side switching has been proposed [24]. This converter used the double current-fed structure with active clamp circuit on the primary side and half-bridge circuit on the secondary side so that the converter can be implemented with a less number of power devices. This converter accomplishes zero input current ripple when the primary-side duty cycle is fixed at 0.5. By adjusting the duty cycle of secondary-side switches, the converter controls its output voltage. Nevertheless, the converter undergoes high instantaneous reactive current as the rated power becomes higher. To remove this problem, a double current-fed dc/dc converter using a bidirectional switch on the secondary side has been suggested [25]. The use of the bidirectional switch removes the reactive current while enabling this switch to be switched OFF with almost zero-voltage-switching (ZVS). As a result, the circuit can operate with high efficiency. However, the voltage across resonant capacitors fluctuates widely and even goes negative when the output power goes over the maximum nominal output power; it was selected as 1 kW to hold the effect of almost ZVS turn-OFF at that power level. Then, shortly after the secondary-side switches are switched ON, nonzero voltage across the resonant capacitors unexpectedly drops to zero. This change creates a high current spike across the primary-side switches. This spike would impair the primary-side switches. Thus, the use of the converter in [25] is limited to the low power range (i.e., 0.1 to 1 kW).

To operate the circuit safely at the powers that exceed maximum nominal output power level, we propose a current-fed diode-clamped resonant converter. Main contributions can be summarized as follows:

1) This circuit solves high current spike problem of the conventional converter when the load is above the maximum nominal output power-level while keeping the main circuit features such as high step-up function, ripple-free characteristic, and soft switching capability unchanged.
2) The secondary-side switches can be switched OFF with complete ZVS, and its secondary-side diodes are OFF with ZCS when the output power is over the maximum nominal output power-level.
3) We have analyzed voltage gain, ZVS/ZCS condition, and current/voltage stress on the active power components in detail when the output power is over the maximum nominal output power-level, which is different from the characteristics when the output power is in its nominal range.

A prototype that operates at maximum nominal output power of 1.0 kW and at peak power of 1.2 kW was implemented to demonstrate the analysis and design of the proposed converter.

II. Operation Principles

Fig. 2 shows the circuit diagram of the proposed converter. On the primary side of transformer T, the proposed current-fed diode-clamped resonant converter equips an interleaved boost circuit with an active clamp circuit with L_1, L_2, S_1–S_4, and C_c. On the secondary side of T, it has a diode-clamped resonant circuit with S_5, S_6, D_1, D_2, D_{c1}, D_{c2}, C_{r1}, C_{r2}, and L_r. In Fig. 2, $S_{i'}$, $D_{S'i'}$, $C_{S'i'}$ $(i = 1, \ldots, 6)$ is composed of equivalent model of the switches; $D_{j'}$ $(j = 1, 2)$ is a output diode; $D_{c'j'}$ is a clamp diode; T is a transformer with turn ratio $n = N_s/N_p$, where N_s is the number of turns in the secondary-side winding and N_p is the number of turns in the primary-side winding; L_m is a magnetizing inductor; L_r is a resonant inductor; L_1 and L_2 are input inductors; C_c is an active clamp capacitor; C_{r1} and C_{r2} are resonant capacitors; C_o is an output capacitor; R_o is a resistive load; V_{in} is the input source voltage; V_{Cc} is the clamp capacitor voltage; V_o is the output voltage; v_{pri} is the primary-side voltage source voltage; v_{Cr1} and v_{Cr2} are the voltages across C_{r1}, C_{r2}, respectively; $i_{S'i'}$ is the current through switch $S_{i'}$; i_{Lm} is the magnetizing current; i_{Lr} is the current that flows through L_r.

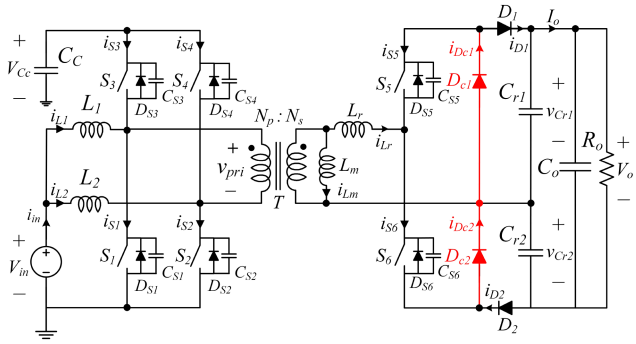

Fig. 2. Schematic diagram of the proposed converter.

(S_1, S_4) and (S_2, S_3) are switched ON and OFF with two pulse-width-modulation (PWM) signals, which have the same $D_p = 0.5$, but are 180° out of phase with each other. S_6 is switched ON after S_1 and S_4 are switched ON, whereas S_5 is switched ON after S_2 and S_3 are switched ON. Once S_5 and S_6 are switched ON, they are switched OFF after $(D_s + 0.5)T_s$. The secondary-side switches of the conventional converter in [25] would suffer from a very high current spike, and so these power devices will be damaged or even destroyed [see (Fig. 3(a)]. In contrast, the proposed converter operates properly without having any current spike at the secondary-side switches [see Fig. 3(b)].

For the purpose of analysis of the proposed converter under steady-state operation, we made several assumptions.

1) $S_1, \ldots, S_6$ are ideal except for $D_{S1}, \ldots, D_{S6}$ and $C_{S1}, \ldots, C_{S6}$. Here, $C_{S1} = \cdots = C_{S4}$, $C_{S5} = C_{S6}$.
2) C_c and C_o are sufficiently large that V_{Cc} and V_o contain no voltage ripple.
3) C_{r1} and C_{r2} are equal; thus, $C_{r1} = C_{r2} = C_r$.
4) L_1 and L_2 are equal; thus, $L_1 = L_2 = L$.

State 1 [t_0, t_1]: S_1, S_4, and S_6 are switched ON at t_0 [see Fig. 4(a)]. S_4 is switched ON with ZVS since C_{S4} is already fully discharged. i_{L1} flows through S_1 and rises linearly as

$$i_{L1}(t) = i_{L1}(t_0) + \frac{V_{in}}{L_1}(t - t_0) \tag{1}$$

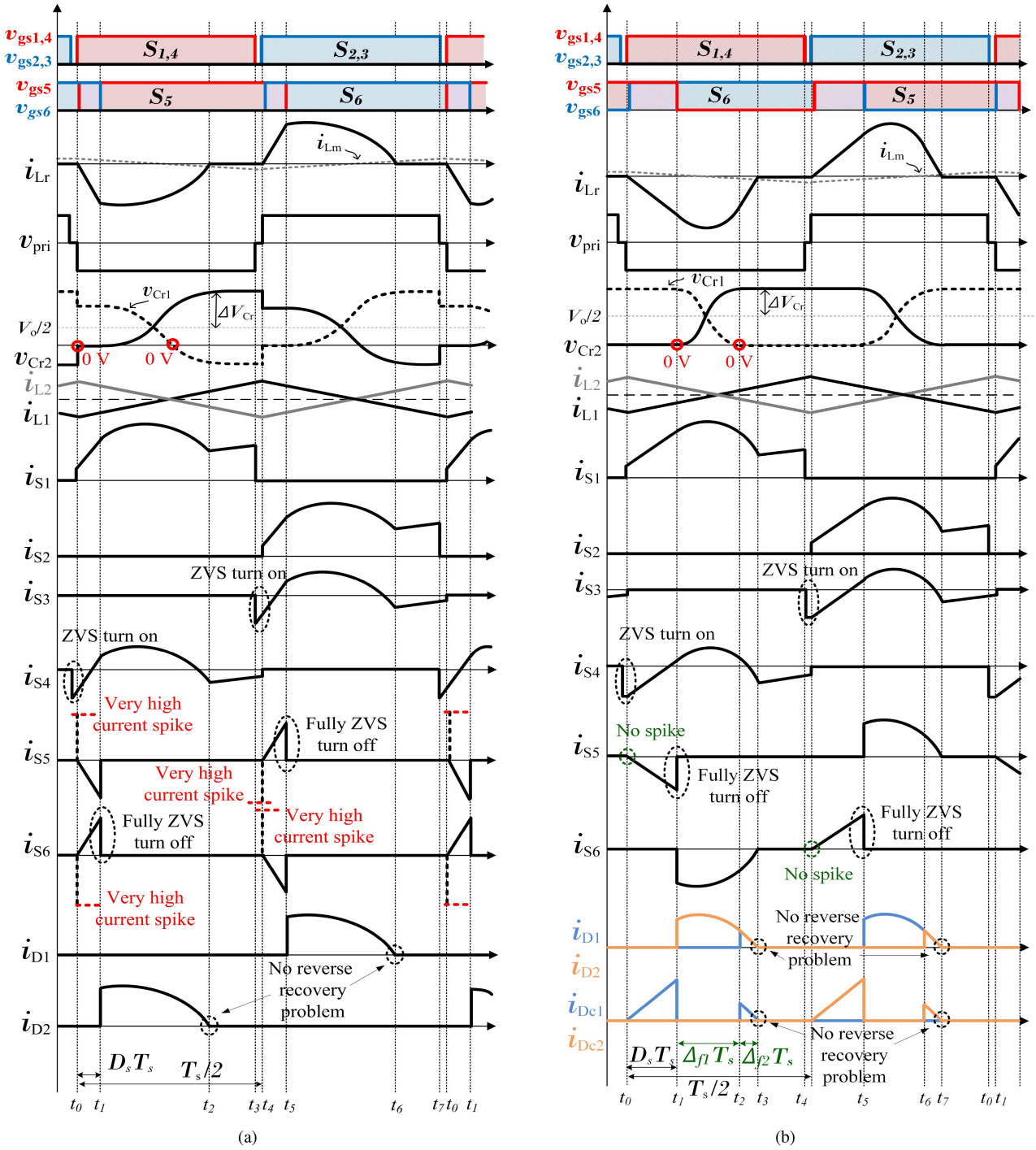

Fig. 3. Key waveforms of the converters that use the secondary-side switching. $v_{gs,'i'}$: the gate-source voltage of the $'i'$th switch. (a) Conventional converter in [25] under $P_o \geq P_{o,nom,\max}$. (b) Proposed converter under $P_o \geq P_{o,nom,\max}$.

and i_{L2} declines linearly as

$$i_{L2}(t) = i_{L2}(t_0) - \frac{(V_{Cc} - V_{in})}{L_2}(t - t_0) \tag{2}$$

v_{pri} is $-V_{Cc}$, which is applied to L_r, so i_{Lr} varies linearly. The state equation is

$$L_r \frac{di_{Lr}(t)}{dt} = -nV_{Cc} \tag{3}$$

with $i_{Lr}(t_0) = 0$.

Solving (3), we have

$$i_{Lr}(t) = \frac{-nV_{Cc}}{L_r}(t - t_0). \tag{4}$$

$v_{Cr1}(t)$ stays at zero. The resonant point follows the path from A_2 to B_2 (see Fig. 5).

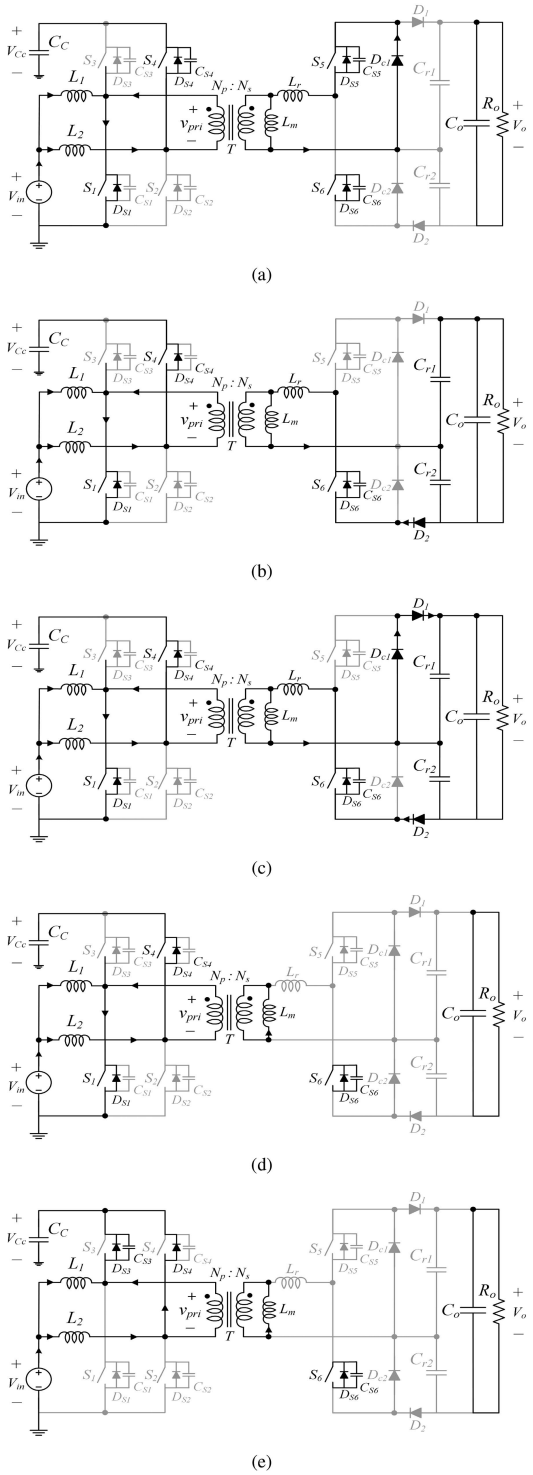

Fig. 4. Equivalent circuits during $T_s/2$. (a) State 1. (b) State 2. (c) State 3. (d) State 4. (e) State 5.

State 2 [t_1, t_2]: S_5 is switched OFF with fully ZVS at t_1 since the applied voltage across S_5 is zero. $-nV_{Cc}$, L_r, C_{r1}, and C_{r2} comprise an equivalent resonant circuit, and i_{Lr} tracks the sinusoidal waveform (see Fig. 3). The state equations are

$$L_r \frac{di_{Lr}(t)}{dt} = -nV_{Cc} - v_{Cr1}(t) + V_o \tag{5}$$

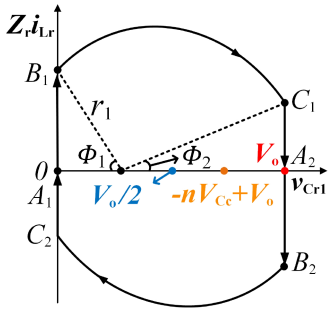

Fig. 5. State-plane path during T_s.

$$i_{Lr}(t) = C_{r1}\frac{dv_{Cr1}(t)}{dt} - C_{r2}\frac{dv_{Cr2}(t)}{dt}. \tag{6}$$

$V_o = v_{Cr1} + v_{Cr2}$, so (6) can be expressed as

$$\begin{aligned} i_{Lr}(t) &= C_{r1}\frac{dv_{Cr1}(t)}{dt} - C_{r2}\frac{d(V_o - v_{Cr1}(t))}{dt} \\ &= 2C_{r1}\frac{dv_{Cr1}(t)}{dt} \end{aligned} \tag{7}$$

with $i_{Lr}(t_1) = -\frac{r_1}{Z_r}\sin\phi_1$ and $v_{Cr1}(t_1) = -nV_{Cc} + V_o + r_1\cos\phi_1$, where $\phi_1 = \sin^{-1}\left(\frac{-nV_{Cc}Z_r}{L_r r_1}(t_1 - t_0)\right)$.

Solving (5) and (6), we have

$$i_{Lr}(t) = -\frac{r_1}{Z_r}\sin[\phi_1 + \omega_r(t - t_1)] \tag{8}$$

$$v_{Cr1}(t) = -nV_{Cc} + V_o + r_1\cos[\phi_1 + \omega_r(t - t_1)] \tag{9}$$

where $r_1 = \frac{V_o}{2} + \Delta V_{Cr} - nV_{Cc}$ is the semidiameter of the round path that has a central point at $(-nV_{Cc} + V_o, 0)$ (see Fig. 5), $Z_r = \sqrt{L_r/(2C_r)}$, and $\omega_r = 1/\sqrt{2L_rC_r}$. ΔV_{Cr} is the voltage ripple of the resonant capacitor. The resonant point follows the path from B_2 to C_2 (see Fig. 5).

State 3 [t_2, t_3]: $nV_{Cc} - V_o$ is applied to L_r at t_2 [see Fig. 4(c)]; i_{Lr} decreases linearly. The state equation is

$$L_r\frac{di_{Lr}(t)}{dt} = nV_{Cc} - V_o \tag{10}$$

with $i_{Lr}(t_0) = \frac{V_o - nV_{Cc}}{L_r}(t_3 - t_2)$.

Solving (10) for $i_{Lr}(t)$, we have

$$i_{Lr}(t) = \frac{V_o - nV_{Cc}}{L_r}(t - t_2) - \frac{V_o - nV_{Cc}}{L_r}(t_3 - t_2). \tag{11}$$

Meanwhile, $v_{Cr1}(t)$ stays at V_o. The resonant point follows the path from C_2 to A_1 (see Fig. 5).

State 4 [t_3, t_4]: $i_{Lr} = 0$ and v_{Cr1} is at its minimum at t_3 [see Fig. 4(d)]. i_{L1} keeps increasing and i_{L2} keeps decreasing. D_1, D_2, and D_{c1} are OFF with ZCS, and so it does not encounter the reverse recovery current. The resonant point stays at A_1 (see Fig. 5).

State 5 [t_4, t_5]: The circuit moves in the dead-time zone at t_4 [see Fig. 4(e)]; S_1 and S_4 are switched OFF. C_{S4} is already fully discharged, so S_4 is switched OFF with ZVS. The resonant point also stays at A_1 during this interval.

III. Analysis At the Steady State

A. Voltage Conversion Ratio When $P_o \geq P_{o,nom,\max}$

In this section, we first define the maximum nominal output power. When the output power is at maximum nominal power level, ΔV_{Cr} defined in [25] is equal to $V_o/2$. Thus,

$$\Delta V_{Cr} = \frac{V_o}{2} = \frac{P_{o,nom,\max} T_s}{2 V_o C_r}. \tag{12}$$

Employing the voltage-second balance law to L_i provides

$$V_{in} \cdot 0.5T_s + (V_{in} - V_{Cc}) \cdot 0.5T_s = 0. \tag{13}$$

Rearranging (13) gives

$$V_{Cc} = 2V_{in}. \tag{14}$$

Kim et al. [25] provided its voltage conversion ratio under $P_o \leq P_{o,nom,\max}$. The proposed converter operates the same as in [25] under $P_o \leq P_{o,nom,\max}$, but differently under $P_o > P_{o,nom,\max}$, so, in this article, we compute the voltage conversion ratio only under $P_o > P_{o,nom,\max}$. The voltage-doubler operates symmetrically; the average value of i_{Lr} becomes twice the average value of I_o. Then, I_o can be obtained as

$$\begin{aligned} I_o &= \frac{P_o}{V_o} \\ &= \frac{2}{T_s}\left[\int_{t_1}^{t_2} \frac{r_1}{2Z_r}\sin[\phi_1 + \omega_r(\tau - t_1)]\,d\tau\right] + \frac{2}{T_s}\left[\int_{t_2}^{t_3} \left(-\frac{V_o - nV_{Cc}}{L_r}(\tau - t_2) + \frac{V_o - nV_{Cc}}{L_r}(t_3 - t_2)\right)d\tau\right] \\ &= \frac{r_1}{T_s Z_r \omega_r}(\cos[\phi_1 + \omega_r(t_2 - t_1)] + \cos\phi_1) + \frac{V_o - nV_{Cc}}{L_r T_s} \cdot (t_3 - t_2)^2. \end{aligned} \tag{15}$$

Using $r_1(\cos[\phi_1 + \omega_r(t_2 - t_1)] + \cos\phi_1) = V_o$ [see Fig. 5] and $(t_3 - t_2) = \Delta_{f2} T_s$ [see Fig. 4(c) to (15)], we obtain

$$I_o = \frac{P_o}{V_o} = \frac{V_o}{T_s Z_r \omega_r} + \frac{V_o - nV_{Cc}}{L_r T_s}(\Delta_{f2} T_s)^2. \tag{16}$$

At t_2, $i_{Lr}(t)$ and $v_{Cr1}(t)$ in state 2 are equal to those in state 3, which presents

$$i_{Lr}(t_2) = \frac{V_o - nV_{Cc}}{L_r}\Delta_{f2} = \frac{r_1}{Z_r}\sin\left[\phi_1 + \omega_r(t_2 - t_1)\right] \tag{17}$$

$$v_{Cr1}(t_2) = V_o = nV_{Cc} - r_1\cos\left[\phi_1 + \omega_r(t_2 - t_1)\right]. \tag{18}$$

Using $\sin^2[\phi_1 + \omega_r(t_2 - t_1)] + \cos^2[\phi_1 + \omega_r(t_2 - t_1)] = 1$, (17) and (18), we obtain

$$\Delta_{f2} = \frac{L_r}{Z_r(V_o - nV_{Cc})T_s}\sqrt{{r_1}^2 - (nV_{Cc} - V_o)^2}. \tag{19}$$

Substituting (19) into (16) yields

$$r_1 = \sqrt{\frac{\left(\frac{P_o}{V_o} - \frac{V_o}{T_s Z_r \omega_r}\right)\cdot\frac{L_r T_s}{V_o - nV_{Cc}}}{\left(\frac{L_r}{Z_r(V_o - nV_{Cc})}\right)^2} + (nV_{Cc} - V_o)^2}. \tag{20}$$

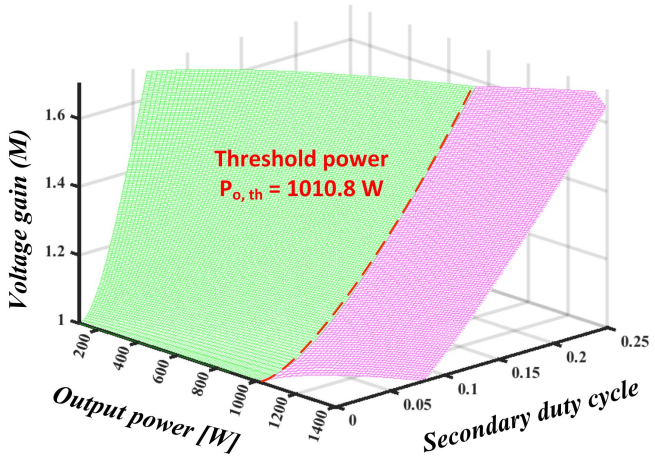

Fig. 6. Voltage conversion ratio of the proposed converter. Green surface: the voltage conversion ratio under $P_o \leq P_{o,nom,\max}$; magenta surface: the voltage conversion ratio under $P_o > P_{o,nom,\max}$.

At t_1, $i_{Lr}(t)$ and $v_{Cr1}(t)$ in state 1 are equal to those in state 2. Using this relationship gives

$$i_{Lr}(t_1) = \frac{nV_{Cc}}{L_r} D_s T_s = \frac{r_1}{Z_r}\sin\phi_1 \tag{21}$$

$$v_{Cr1}(t_1) = 0 = nV_{Cc} - r_1\cos\phi_1. \tag{22}$$

Using $\sin^2\phi_1 + \cos^2\phi_1 = 1$, (21), and (22), we obtain

$$D_s = \frac{L_r r_1}{nV_{Cc} Z_r T_s}\sqrt{1 - \left(\frac{nV_{Cc}}{r_1}\right)^2}. \tag{23}$$

Substituting (20) into (23) yields

$$D_s = \frac{2M}{T_s V_o}\sqrt{L_r\left[T_s P_o - \frac{1}{2M}(V_o^2 C_r + T_s P_o)\right]} \tag{24}$$

where $M = V_o/2nV_{Cc}$ is the voltage conversion ratio of the proposed converter. Rearranging (24) with regard to M, we have

$$M = \frac{1}{2} + \frac{{V_o}^2 C_r}{2T_s P_o} + \frac{D_s T_s V_o}{2\sqrt{L_r T_s P_o}}. \tag{25}$$

The variation of M with respect to D_s and P_o becomes more stiff when $P_o > P_{o,nom,\max}$ (see Fig. 6).

Δ_{f1} can be obtained as follows. Utilizing $(t_2 - t_1) = \Delta_{f1}$ (see Fig. 3) to (8) and (9) yields $i_{Lr}(t)$ and $v_{Cr1}(t)$ at t_2

$$i_{Lr}(t_2) = \frac{r_1}{Z_r}\sin\left[\phi_1 + \omega_r(t_2 - t_1)\right] = \frac{V_o - nV_{Cc}}{L_r}(t_3 - t_2) \tag{26}$$

$$v_{Cr1}(t_2) = nV_{Cc} - r_1\cos\left[\phi_1 + \omega_r(t_2 - t_1)\right] = V_o \tag{27}$$

then using $\cos(\phi_1 + \phi_2) = \cos\phi_1\cos\phi_2 - \sin\phi_1\sin\phi_2$ in (27) yields

$$\cos(\omega_r \Delta_{f1} T_s) = \frac{1}{nV_{Cc}}\left[nV_{Cc} - V_o + \frac{nV_{Cc} D_s T_s Z_r \sin(\omega_r \Delta_{f1} T_s)}{L_r}\right]. \tag{28}$$

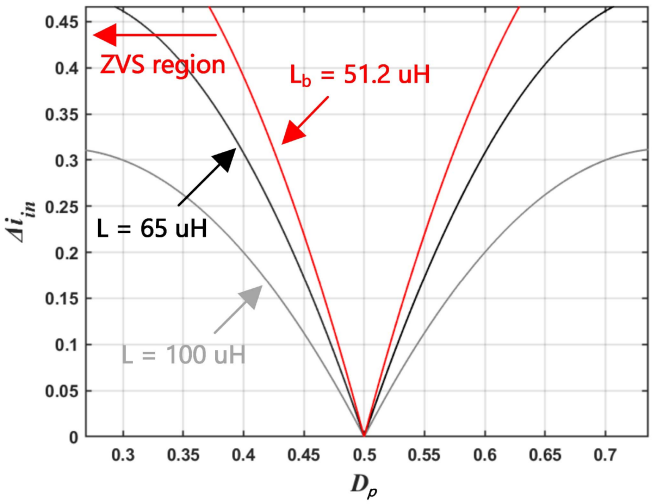

Fig. 7. Normalized input-current ripple of the proposed converter with regard to the variation of D_p. L_b is the minimum value of the input inductance for ZVS turn-OFF for S_3 and S_4.

Using $\sin(\phi_1+\phi_2)=\cos\phi_1\sin\phi_2+\sin\phi_1\cos\phi_2$ and (28) in (26) yields

$$\Delta_{f1}=\frac{1}{T_s\omega_r}\sin^{-1}\left[\frac{T_s(V_o-nV_{Cc})(\Delta_{f2}+D_s)}{\left(D_s^2T_s^2\omega_r+\frac{1}{\omega_r}\right)\cdot nV_{Cc}}\right]. \quad (29)$$

B. Input Current Ripple When $P_o \geq P_{o,nom,\max}$

For a given $L_1=L_2=L$, the high-frequency current ripples on each inductor and at the input are presented as

$$\Delta i_{L1}=\Delta i_{L2}=\frac{V_{in}\cdot(1-D_p)\cdot D_p\cdot T_s}{L} \quad (30)$$

$$\Delta i_{in}=\begin{cases}\frac{V_{in}\cdot D_p\cdot(1-2D_p)\cdot T_s}{L}, & \text{if } D_p\leq 0.5\\ \frac{V_{in}\cdot D_p\cdot(2D_p-1)\cdot T_s}{L}, & \text{if } D_p>0.5.\end{cases} \quad (31)$$

The normalized $\Delta i_{L1,2}$ and Δi_{in} versus D_p vary according to (30) and (31) (see Fig. 7); D_p is set to be 0.5; i_{L1} and i_{L2} are 180° out of phase with each other, and are merged at the input; the high-frequency input current ripple becomes theoretically zero, which can extend the life-span of the fuel-cell.

IV. Design Considerations

A. Determine Value of Input Inductance

To ensure ZVS turn OFF for S_3 and S_4, Δi_{in} needs to be less than the average current I_{in}, or

$$\Delta i_{in}=\frac{V_{in}}{4\,Lf_s}\leq\frac{P_o}{2\eta V_{in}}=I_{in} \quad (32)$$

where η is the efficiency of the converter and P_o is its output power

$$L\geq\frac{\eta {V_{in\_\max}}^2}{2P_of_s}=\frac{1\cdot 72^2}{2\cdot 1,200\cdot 50,000}=43.2\ \mu\text{H} \quad (33)$$

where $V_{in\_\max}$ is the maximum value of V_{in}.

According to (33), we set $L_1=L_2=65\ \mu$H.

B. Determine Values of Resonant Inductance and Capacitance

Rearranging (12) with regard to C_r, we have

$$C_r=\frac{P_{o,nom,\max}T_s}{V_o^2}=\frac{1,010.8\times 0.00002}{380^2}=140\ \text{nF}. \quad (34)$$

Using $w_r=1/\sqrt{L_rC_r}$ expected to be slightly higher than angular switching frequency and (34), we have

$$L_r\leq\frac{V_o^2}{\omega_r^2P_{o,nom,\max}T_s}=\frac{380^2}{(2\pi\times 51,000)^2\times 1,010.8\times 0.00002}=69.6\ \mu\text{H}. \quad (35)$$

Furthermore, the converter needs to meet the following condition to satisfy ZCS turn OFF for the diodes:

$$D_s+\Delta_{f1}+\Delta_{f2}<0.5 \quad (36)$$

Rearranging (36) with regard to L_r, we have (37) shown at the bottom of this page. To achieve ZCS, L_r should satisfy (37). We have obtained ZCS region of the proposed converter according to (37) (see Fig. 8). The maximum value of L_r to meet ZCS condition under the operating region is 27.4 μH. Thus, we set L_r as 25.5 μH.

C. Selection of Active Power Devices

Primary-side active power devices experience a maximum voltage stress of V_{Cc} and secondary-side active power devices suffer from a maximum voltage stress of V_o. Peak currents of active power devices can be written as

$$I_{S1,2,pk}=\frac{n^2V_{Cc}T_s}{4}\cdot\left(\frac{1}{L_r}-\frac{1}{L_m}\right)+\frac{T_s}{4}\cdot\left(\frac{V_{in}}{L_1}+\frac{P_o}{2V_{in}}\right) \quad (38)$$

$$I_{S3,4,pk}=\frac{n^2V_{Cc}T_s}{4}\cdot\left(\frac{1}{L_r}-\frac{1}{L_m}\right)-\frac{T_s}{4}\cdot\left(\frac{V_{in}}{L_1}+\frac{P_o}{2V_{in}}\right) \quad (39)$$

$$I_{S5,6,pk}=\frac{nV_{Cc}}{L_r}\cdot D_sT_s \quad (40)$$

$$I_{D1,2,pk}=\frac{r_1}{Z_r}\sin\left[\phi_1+w_r(t-t_1)\right] \quad (41)$$

$$L_r<\frac{0.25}{\left(\frac{2M}{T_sV_o}\sqrt{\left(T_sP_o-\frac{(V_o^2C_r+T_sP_o)}{2M}\right)}+\frac{\sqrt{C_r}}{T_s}\sin^{-1}\left(\frac{T_s(V_o-nV_{Cc})(\Delta_{f1}+D_s)}{nV_{Cc}\cdot\left(D_s^2T_s^2\omega_r+\frac{1}{\omega_r}\right)}\right)+\frac{\sqrt{C_r}\sqrt{r_1^2-(nV_{Cc}-V_o)^2}}{T_s(V_o-nV_{Cc})}\right)^2}. \quad (37)$$

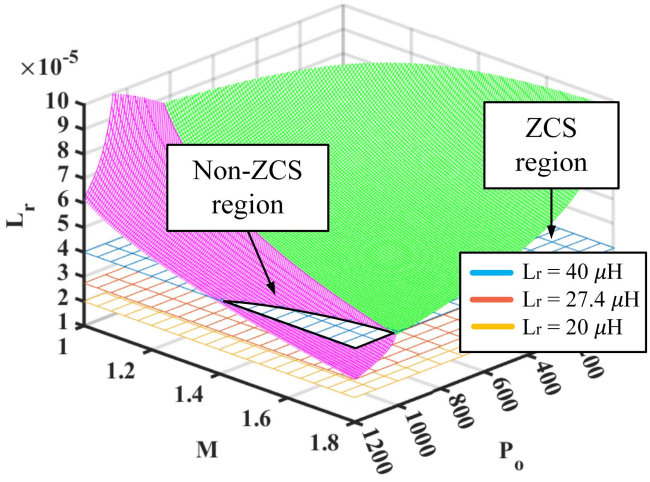

Fig. 8. ZCS condition for the diodes. Green surface: the boundary of L_r to satisfy ZCS condition with regard to the voltage conversion ratio and output power under $P_o \le P_{o,nom,\max}$; magenta surface: the boundary of L_r under $P_o > P_{o,nom,\max}$.

TABLE I
COMPONENT RATINGS AND DEVICES OF THE PROPOSED CONVERTER

Devices	Ratings	Devices
S_1, S_2	$I_{S1,2,pk} \approx 30$ A $V_{S1,2,pk} \approx 144$ V	IPP051N15N5
S_3, S_4	$I_{S3,4,pk} \approx 11$ A $V_{S3,4,pk} \approx 144$ V	IPP051N15N5
S_5, S_6	$I_{S5,6,pk} \approx 17.3$ A $V_{S5,6,pk} \approx 380$ V	UJ3C065030K3S
D_1, D_2	$I_{D1,2,pk} \approx 17.3$ A $V_{D1,2,pk} \approx 380$ V	60CPU04
D_{c1}, D_{c2}	$I_{Dc1,c2,pk} \approx 11$ A $V_{Dc1,c2,pk} \approx 380$ V	60CPU04

$$I_{Dc1,c2,pk} = \frac{nV_{Cc}}{L_r} \cdot D_s T_s. \tag{42}$$

Component ratings and devices were selected as in Table I.

Remark 1: We selected $C_r = 70$ nF to make $\Delta V_{Cr} \simeq V_o/2$ at the maximum nominal output power of 1 kW. Then, S_5 and S_6 are turned OFF with 4.38 V at $P_o = 1$ kW; the corresponding switching loss at turn-OFF instant becomes negligible (see Fig. 9). The voltage stress on the secondary-side switches is high but it is still less than V_o. Thanks to the use of two clamp diodes, the proposed circuit can operate without having any problem under 20% overloaded environment. If we select $C_r = 83$ nF to make $\Delta V_{Cr} \simeq V_o/2$ at the maximum nominal output power of 1.2 kW, S_5 and S_6 are turned OFF with 40.4 V at $P_o = 1$ kW. Thus, the corresponding switching loss at turn-OFF instant is not negligible (see Fig. 9). If we make C_r much larger, the corresponding switching loss at turn-OFF instant becomes much higher.

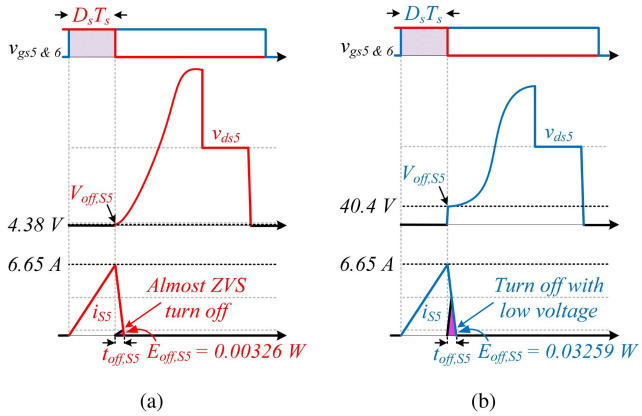

Fig. 9. Turn-OFF voltage variation at the secondary-side switch S_5 as the values of $P_{o,nom\_\max}$ and C_r change. (a) Waveforms of the circuit when $P_{o,nom\_\max} = 1$ kW and $C_r = 70$ nF. (b) Waveforms of the circuit when $P_{o,nom\_\max} = 1.2$ kW and $C_r = 83$ nF.

TABLE II
SELECTED PARAMETERS FOR THE PROPOSED CONVERTER

Parameters	Symbols	Value
Input voltage	V_{in}	48−72 V
Desired output voltage	$V_{o,ref}$	380 V
Maximum nominal output power	P_{o,nom_max}	1.0 kW
Peak output power	$P_{o,peak}$	1.2 kW
Switching frequency	f_s	50 kHz
Resonant frequency	f_r	84 kHz
Input inductor	$L_{1,2}$	65 μH
Resonant inductance	L_r	25.5 μH
Magnetizing inductance	L_m	360 μH
Clamp capacitance	C_C	20 μF
Transformer turns ratio	N_p:N_s	30:38
Resonant capacitance	C_{r1}, C_{r2}	70 nF
Output capacitance	C_o	120 μF

V. EXPERIMENTAL RESULTS AND DISCUSSION

A 1.2-kW laboratory prototype (see Table II, Fig. 10) of the proposed converter has been built and operated to prove the proposed concept. We conducted experimental tests for the proposed converter under $48 \le V_{in} \le 72$ V, $V_{o,ref} = 380$ V, and $P_o = 1.2$ kW. A control algorithm was developed on Code Composer Studio program and carried out with a TMS320F28377 digital signal processor; this processor transmits the control signal to the embedded control peripherals.

S_5 of the converter [25] does not experience a large current spike at $P_o = 1$ kW, but undergoes a large current spike above the maximum nominal output power, i.e., $P_o = 1.2$ kW [see

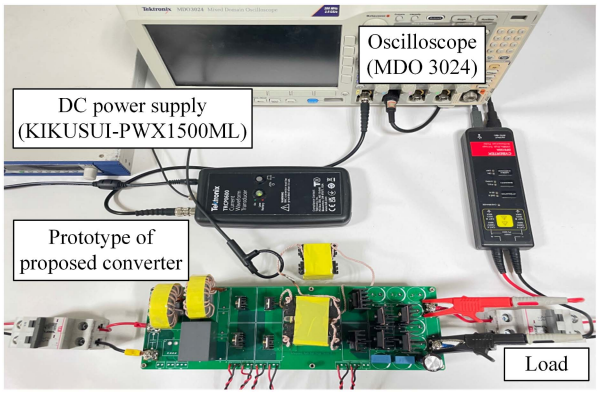

Fig. 10. Experimental setup of the proposed converter.

Fig. 11(a), (b)]; it is up to 500 A in the simulation; the magnitude of the current spike can be reduced according to the value of output capacitance of S_5. On the contrary, the proposed converter showed no spike even at $P_o = 1.2$ kW [see Fig. 11(c), (d)]. In the proposed converter, i_{Lr} rises linearly when S_5 and S_6 are switched ON. After S_5 or S_6 is switched OFF, i_{Lr} flows sinusoidally. After v_{Cr1} reaches zero, i_{Lr} declines linearly and stays at zero (see Fig. 12). Experimental waveforms of i_{S1} with v_{gs1} and v_{gs6} (see Fig. 13) were in close agreement with theoretical waveforms. S_4 is switched ON with ZVS (see Fig. 14). i_{S5} rises linearly whereas S_5 is switched ON (see Fig. 15). After S_5 is switched OFF, v_{ds5} at the turn-OFF instant becomes zero thanks to the voltage swing across the resonant capacitor. Thus, we can achieve turn OFF with complete ZVS at S_5.

Right after S_5 is switched OFF, the sinusoidal current flows through D_1 (see Fig. 16). At the end, D_1 is OFF with ZCS and does not suffer from the reverse-recovery current. When $v_{Cr2} = 0$, the linear current flows through D_{c1}. At the end, D_{c1} is also OFF without the reverse-recovery current. The high-frequency ripples of i_{L1} and i_{L2} become symmetric (see Fig. 17). When they are merged, they cancel each other.

The efficiency of the proposed converter is assessed by Yokogawa WT1800E digital power meter. Its maximum efficiency is 95.8% at 700 W when input voltage is 72 V (see Fig. 18). The efficiencies at full load are 92.9% at $V_{in} = 48$ V and 94.3% at $V_{in} = 72$ V.

In Fig. 19, the loss at transformer T, the loss at inductors L_r and $L_{1,2}$ and the conduction loss at diodes $D_{c1,c2}$ and $D_{1,2}$ take 11.3 W, 6.1 W + 2.1 W, and 2.0 W + 3.4 W at $V_{in} = 48$ V and at $P_o = 700$ W; 5.3 W, 2.5 W + 3.5 W, and 0.1 W + 3.4 W at $V_{in} = 72$ V and at $P_o = 700$ W; 28.0 W, 10.8 W + 2.4 W, and 4.5 W + 5.8 W at $V_{in} = 48$ V and at full load; 15.5 W, 6.9 W + 2.7 W, 1.5 W + 6.0 W at $V_{in} = 72$ V and at full load; these losses are dominant in the proposed converter. To reduce the losses occurred at $D_{c1,c2}$ and $D_{1,2}$, we can replace the clamp diodes or output diodes by the switches and adopt the synchronous rectification (SR) operation. For SR operation at the place of the output diodes, we need to turn ON these switches by checking the rising edge of the resonant current and falling edge of the current. On the other hand, two triangular currents will flow through the switches at the place of the clamp diodes. To achieve SR operation, we need to turn ON these switches during the turn-ON duty period of S_5 or S_6 for the first triangular current. Then, we need to turn ON these switches by checking the rising edge of the second triangular current and falling edge of the current. We have obtained detailed loss distribution without SR operation, with SR operation for the clamp diodes and with SR operation for the clamp diodes and output diodes at $P_o = 700$ W and at full

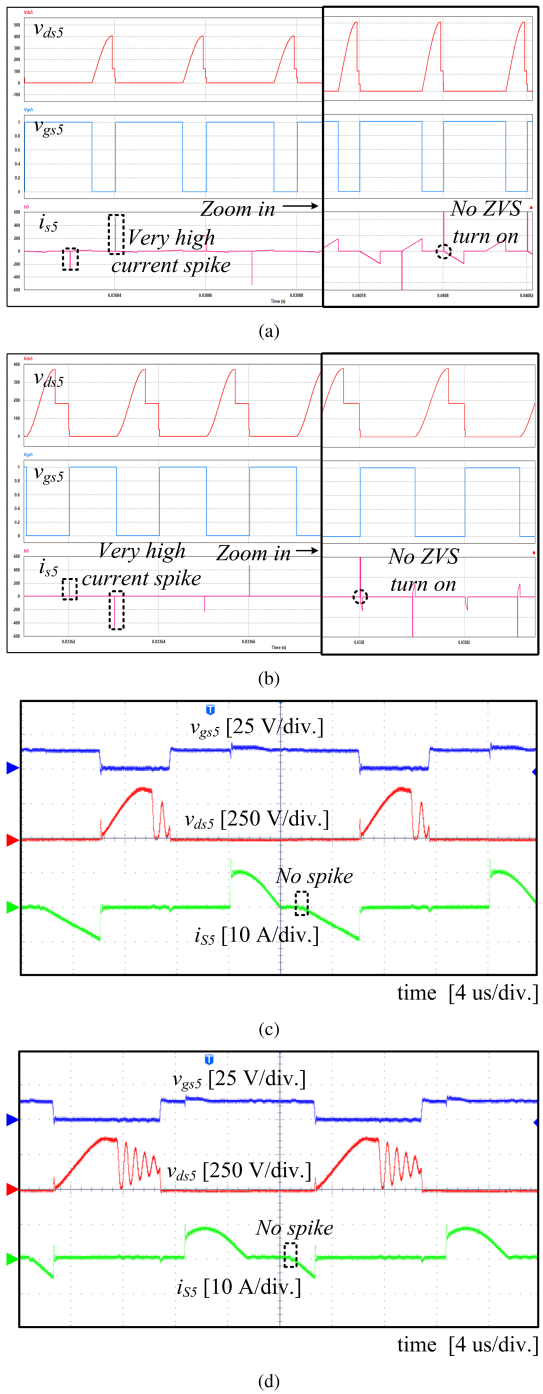

Fig. 11. Waveforms of v_{gs5}, v_{ds5}, i_{s5} in the conventional converter [25] and proposed converter under $P_o \geq P_{o,nom,\max}$. (a) Simulation waveform at $V_{in} = 48$ V. (b) Simulation waveform at $V_{in} = 72$ V. (c) Experimental waveform at $V_{in} = 48$ V. (d) Experimental waveform at $V_{in} = 72$ V.

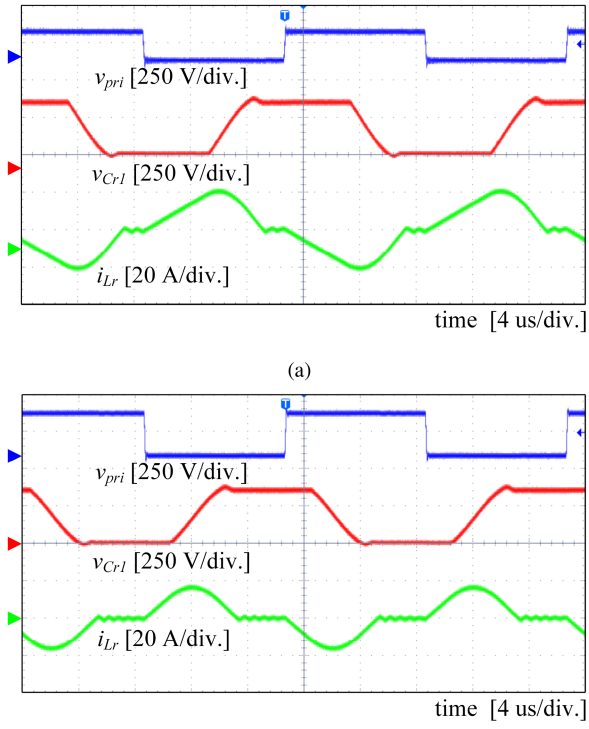

Fig. 12. Experimental waveforms of v_{pri} with v_{Cr1} and i_{Lr} at $P_o = 1.2$ kW. (a) At $V_{in} = 48$ V. (b) At $V_{in} = 72$ V.

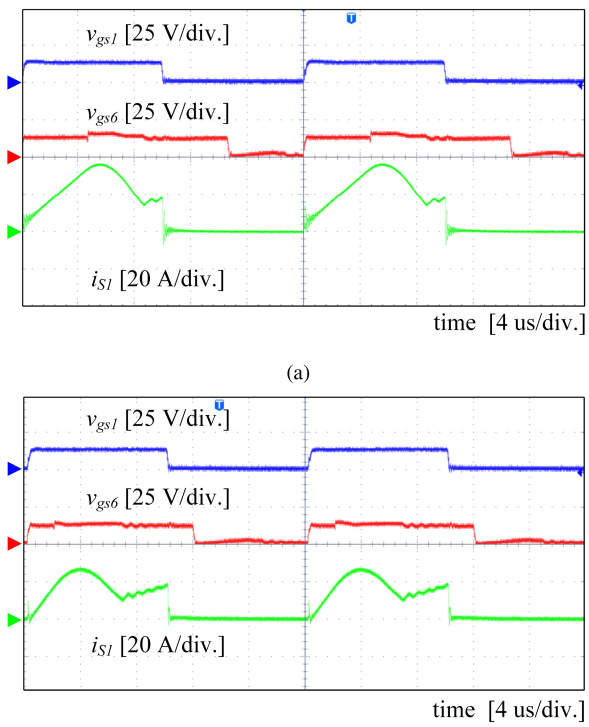

Fig. 13. Experimental waveforms of i_{S1} with v_{gs1} and v_{gs6} at $P_o = 1.2$ kW. (a) At $V_{in} = 48$ V. (b) At $V_{in} = 72$ V.

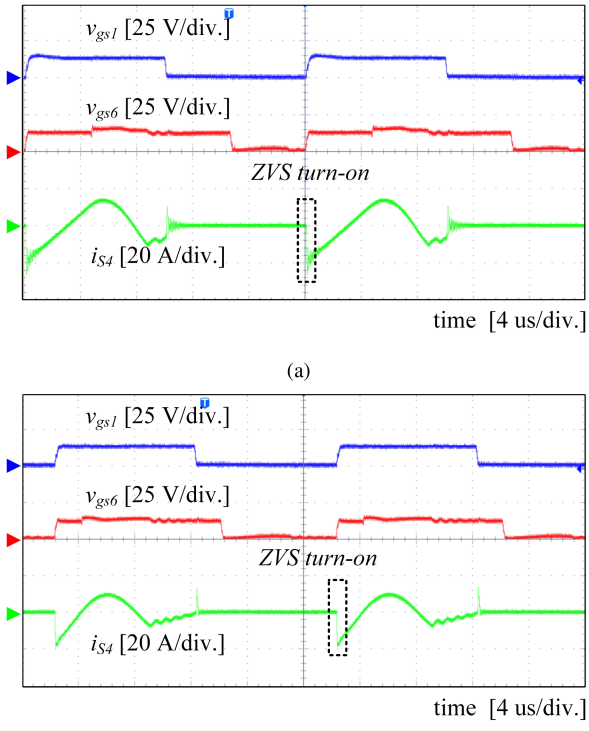

Fig. 14. Experimental waveforms of i_{S4} with v_{gs1} and v_{gs6} at $P_o = 1.2$ kW. (a) At $V_{in} = 48$ V. (b) At $V_{in} = 72$ V.

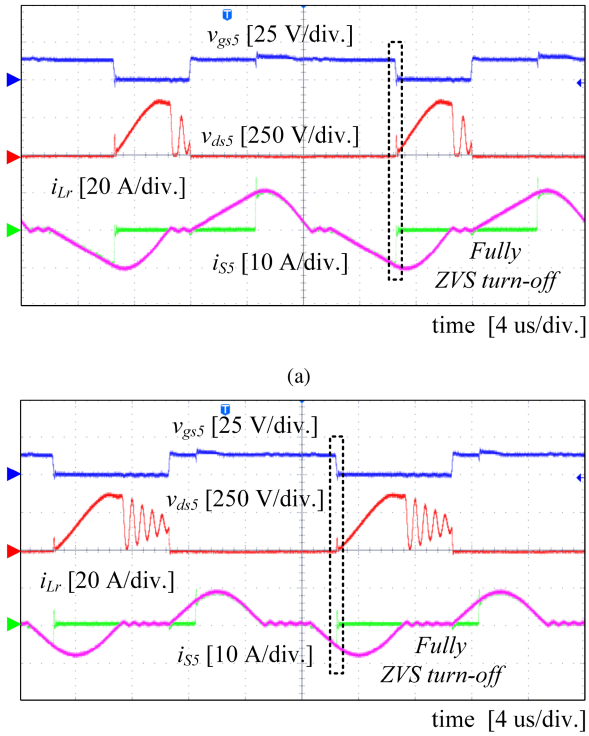

Fig. 15. Experimental waveforms of i_{S5} with v_{ds5} and v_{gs5} at $P_o = 1.2$ kW. (a) At $V_{in} = 48$ V. (b) At $V_{in} = 72$ V.

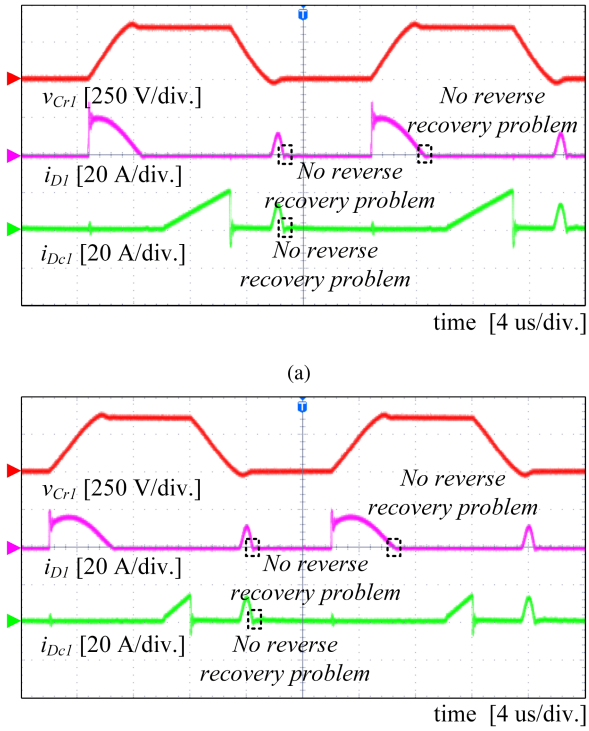

Fig. 16. Experimental waveforms of v_{Cr1} with i_{D1} and i_{Dc1} at $P_o = 1.2$ kW. (a) At $V_{in} = 48$ V. (b) At $V_{in} = 72$ V.

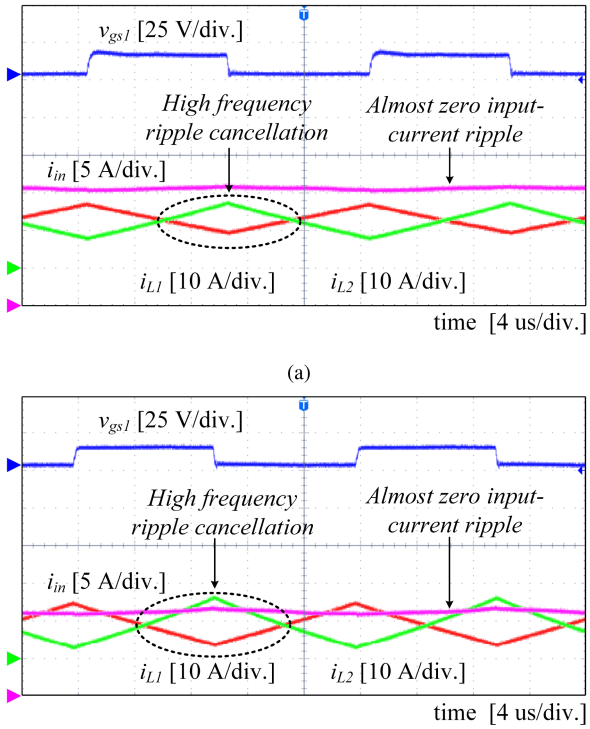

Fig. 17. Experimental waveforms of i_{in}, i_{L1}, and i_{L2} with v_{gs1} at $P_o = 1.2$ kW. (a) At $V_{in} = 48$ V. (b) At $V_{in} = 72$ V.

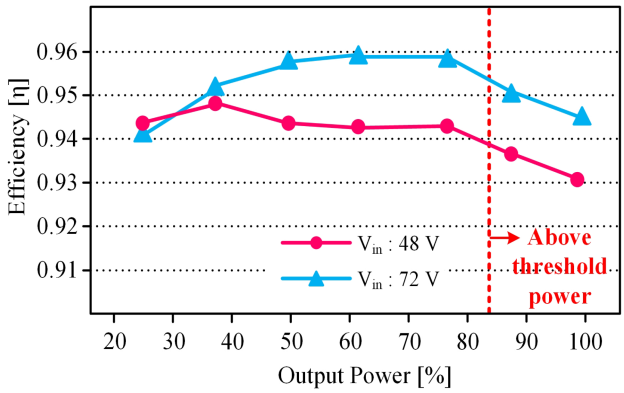

Fig. 18. Measured efficiency η of the proposed converter for V_{in} =48 V/72 V and $V_o = 380$ V.

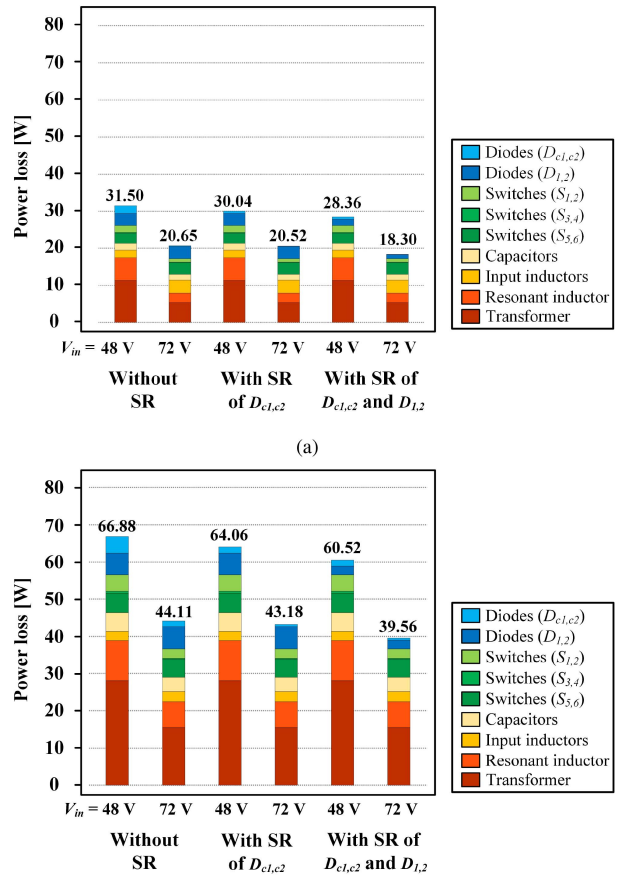

Fig. 19. Theoretical power loss distribution of the proposed converter without SR operation, with SR operation of $D_{c1,c2}$, and with SR operation of $D_{c1,c2}$ and $D_{1,2}$. (a) At $P_o = 700$ W. (b) At full load.

load. SR operation for the clamp diodes results in an increase in efficiency by 0.01% at $P_o = 700$ W load and by 0.1% at full load. SR operation for the clamp diodes and the output diodes results in an increase in efficiency by 0.23% at $P_o = 700$ W and by 0.4% at full load. From this result, we can deduce that the experimental peak efficiency of the proposed converter occurred

TABLE III
COMPARISON OF THE PROPOSED CONVERTER AND THE CONVENTIONAL CURRENT-FED CONVERTERS THAT USE SECONDARY-SIDE SWITCHING

Items		[23]	[24]	[25]	Proposed
Topology		Double current-fed full bridge + bridgeless rectifier	Double current-fed full bridge + active voltage douber	Double current-fed full bridge + voltage doubler employing bidirectional switch	Double current-fed full bridge + diode-clamped cell
Input voltage		35–45 V	35–45 V	48–72 V	48–72 V
Output voltage		380 V	380 V	380 V	380 V
Power rating		600 W	600 W	1 kW	1.2 kW (>1 kW)
Inductor current	State 1	Linear	Resonant	Linear	Linear
	State 2	Resonant	Resonant	Resonant	Resonant
	State 3	–	–	–	Linear
Voltage conversion ratio		$2n\frac{1+\sqrt{1-(A^2-1)B}}{1+A}$	$\frac{A+B+\sqrt{(1-4B)A^2+6AB+B^2}}{2B(1-A)}$	$1+\frac{D_sV_s}{2}\sqrt{\frac{T_s}{L_rP_s}}$	$\frac{1}{2}+\frac{{V_o}^2C_r}{2T_sP_o}+\frac{D_sT_sV_o}{2\sqrt{L_rT_sP_o}}$
Values of power devices	Switching frequency	50 kHz	50 kHz	50 kHz	50 kHz
	Resonant frequency	25.3 kHz	50.2 kHz	60 kHz	84.23 kHz
	Transformer turns ratio	12:44	13:24	15:19	30:38
	Resonant inductance	77.9 μH	35.6 μH	36.8 μH	25.5 μH
	Resonant capacitance	200 nF	141 nF	200 nF	140 nF
	Output capacitance	20 μF	20 μF	100 μF	120 μF
Number of components	Switches	6	6	6	6
	Diodes	2	0	2	4
	Capacitors	3	3	3	3
	Inductors	3	3	3	3
	Transformers	1	1	1	1
Peak efficiency		96.2%	97.3%	96.8%	95.8%
Operation when $P_o > P_{o,nom,max}$		Invulnerable	Vulnerable	Vulnerable	Invulnerable

A and B are defined in [23], [24].

at $P_o = 700$ W can be upto 96.1%, which is similar to the peak efficiency of [23].

The proposed and existing double current-fed isolated resonant converters that used secondary-side switching have different numbers of devices and characteristics of electrical output (see Table III). The converter that used the bridgeless rectifier on the secondary side of the circuit [23] has been suggested. It can step up the output voltage further using the secondary-side switching, but the secondary-side switches are turned OFF with hard switching. Also, it cannot enjoy the voltage gain of two obtained from the use of voltage doubler. The converter that used the active-voltage doubler on the secondary side of the circuit [24] can be developed with small number of active power devices, but its instantaneous reactive current becomes higher when the duty-ratio becomes higher; this trait decreases the efficiency. The converter proposed in [25] adopted the voltage doubler with the bidirectional switch on the secondary side. It exhibits nearly ZVS turn OFF on the secondary-side of the switches, and so the efficiency is high. However, when the output power goes above the maximum nominal output power, the circuit undergoes a severe current spike, which can impair the semiconductor devices. To remove the current spike, the proposed converter adopted diode-clamped cell on the secondary side. The use of the diode-clamped cell enables the secondary-side switches to be OFF with complete ZVS when the output power is above its nominal value.

VI. Conclusion

This article presents the high step-up current-fed diode-clamped resonant converter for overloaded fuel-cell vehicles. By incorporating the diode-clamped cell at the secondary side of the transformer, the proposed converter guarantees stable operation above the maximum nominal output power while retaining the benefits of the conventional converter such as high step-up function, zero high-frequency ripple, and soft-switching capability. When the output power is over its nominal value, the secondary-side switches are switched OFF with complete ZVS and its secondary-side diodes are OFF with ZCS. A 1.2-kW prototype was implemented and tested to justify the superior operation characteristics of the proposed converter.

Acknowledgment

The authors are thankful to human resources development project of the Korea Institute of Energy Technology Evaluation and Planning (KETEP) for the support grant funded by the Korea government Ministry of Trade, Industry and Energy under the project titled: "Middle market enterprise specialized human resources developme for residential and commercial fuel cell," numbered: 20224000000580.

References

[1] M. Uno and K. Tanaka, "PT/C catalyst degradation in proton exchange membrane fuel cells due to high-frequency potential cycling induced by switching power converters," *J. Power Sources*, vol. 196, no. 23, pp. 9884–9889, Dec. 2011.

[2] J. S. Lai and M. W. Ellis, "Fuel cell power systems and applications," *Proc. IEEE*, vol. 105, no. 11, pp. 2166–2190, Nov. 2017.

[3] B. Han, C. Bai, J. S. Lee, and M. Kim, "Repetitive controller of capacitorless current-fed dual-half-bridge converter for grid-connected fuel cell system," *IEEE Trans. Ind. Electron.*, vol. 65, no. 10, pp. 7841–7855, Oct. 2018.

[4] S. Hasanpour, Y. P. Siwakoti, A. Mostaan, and F. Blaabjerg, "New semiquadratic high step-up DC/DC converter for renewable energy applications," *IEEE Trans. Power Electron.*, vol. 66, no. 1, pp. 433–446, Jan. 2020.

[5] V. R. Vakacharla and A. K. Rathore, "Isolated soft switching current fed LCC-T resonant DC–DC converter for PV/Fuel cell applications," *IEEE Trans. Ind. Electron.*, vol. 66, no. 9, pp. 6947–6958, Sep. 2019.

[6] Y. Zhang et al., "Wide input-voltage range boost three-level DC–DC converter with quasi-Z source for fuel cell vehicles," *IEEE Trans. Power Electron.*, vol. 32, no. 9, pp. 6728–6738, Sep. 2020.

[7] A. Chub, D. Vinnikov, E. Liivik, and T. Jalakas, "Multiphase quasi-Z-source DC–DC converters for residential distributed generation systems," *IEEE Trans. Ind. Electron.*, vol. 65, no. 10, pp. 8361–8371, Oct. 2018.

[8] M. M. Haji-Esmaeili, E. Babaei, and M. Sabahi, "High step-upquasi-Z source DC–DC converter," *IEEE Trans. Power Electron.*, vol. 33, no. 12, pp. 10563–10571, Dec. 2018.

[9] P. Alavi, P. Mohseni, E. Babaei, and V. Marzang, "An ultra-high step-up DC–DC converter with extendable voltage gain and soft-switching capability," *IEEE Trans. Ind. Electron.*, vol. 67, no. 11, pp. 9238–9250, Nov. 2019.

[10] Y. Yuan, L. Lai, and Q. Wu, "A current-fed LCL resonant converter for wide output-voltage applications," *IEEE Trans. Ind. Electron.*, vol. 68, no. 5, pp. 3939–3948, May 2020.

[11] R. Beiranvand and S. H. Sangani, "A family of interleaved high step-up DC–DC converters by integrating a voltage multiplier and an active clamp circuits," *IEEE Trans. Power Electron.*, vol. 37, no. 7, pp. 8001–8014, Jul. 2022.

[12] M. F. Guepfrih, G. Waltrich, and T. B. Lazzarin, "High step-up DC-DC converter using built-in transformer voltage multiplier cell and dual boost concepts," *IEEE J. Emerg. Sel. Topics Power Electron.*, vol. 9, no. 6, pp. 6700–6712, Dec. 2021.

[13] Y. Gu, Y. Chen, B. Zhang, D. Qiu, and F. Xie, "High step-up DC–DC converter with active switched LC-network for photovoltaic systems," *IEEE Trans. Energy. Convers..*, vol. 34, no. 1, pp. 321–329, Mar. 2019.

[14] G. G. Kumar, K. Sundaramoorthy, V. Karthikeyan, and E. Babaei, "Switched capacitor–inductor network based ultra-gain DC–DC converter using single switch," *IEEE Trans. Ind. Electron.*, vol. 67, no. 12, pp. 10274–10283, Dec. 2020.

[15] Y. Ye, S. Chen, and Y. Yi, "Switched-capacitor and coupled-inductor-based high step-up converter with improved voltage gain," *IEEE J. Emerg. Sel. Topics Power Electron.*, vol. 9, no. 1, pp. 754–764, Feb. 2021.

[16] F. Shang, G. Niu, and M. Krishnamurthy, "Design and analysis of a high-voltage-gain step-up resonant DC–DC converter for transportation applications," *IEEE Trans. Transp. Electrific.*, vol. 3, no. 1, pp. 157–167, Mar. 2017.

[17] N. Swaminathan and Y. Cao, "An overview of high-conversion high-voltage DC–DC converters for electrified aviation power distribution system," *IEEE Trans. Transp. Electrific.*, vol. 6, no. 4, pp. 1740–1754, Dec. 2020.

[18] C. F. Moraes, E. G. Carati, J. P. da Costa, R. Cardoso, and C. M. de Oliveira Stein, "Active-clamped zero-current switching current-fed half-bridge converter," *IEEE Trans. Power Electron.*, vol. 35, no. 7, pp. 7100–7109, Jul. 2020.

[19] J. Liu, K. Wang, Z. Zheng, C. Li, and Y. Li, "A dual-active-clamp quasi-resonant isolated boost converter for PV integration to medium-voltage DC grids," *IEEE J. Emerg. Sel. Topics Power Electron.*, vol. 8, no. 4, pp. 3444–3456, Dec. 2020.

[20] N. Yang, J. Zeng, R. Hu, and J. Liu, "Analysis and design of an isolated high step-up converter without voltage-drop," *IEEE Trans. Power Electron.*, vol. 37, no. 6, pp. 6939–6950, Jun. 2022.

[21] D. Chakraborty, E. Breaz, A. K. Rathore, and F. Gao, "Parasitics-assisted soft-switching and secondary modulated snubberless clamping current-fed bidirectional voltage doubler for fuel cell vehicles," *IEEE Trans. Veh. Technol.*, vol. 66, no. 2, pp. 1053–1062, Feb. 2017.

[22] S. Tandon and A. K. Rathore, "Analysis and design of series LC resonance-pulse based zero-current-switching current-fed half-bridge DC–DC converter," *IEEE Trans. Ind. Electron.*, vol. 68, no. 8, pp. 6784–6793, Aug. 2021.

[23] H. Seok, B. Han, S. H. Kim, J. G. Lee, and M. Kim, "Rippleless resonant boost converter for fuel-cell power conditioning systems," in *Proc. IEEE Appl. Power Electron. Conf. Expo.*, 2018, pp. 653–658.

[24] H. Seok, B. Han, B. H. Kwon, and M. Kim, "High step-up resonant DC–DC converter with ripple-free input current for renewable energy systems," *IEEE Trans. Ind. Electron.*, vol. 65, no. 11, pp. 8543–8552, Nov. 2018.

[25] N. G. Kim, B. Han, S. W. Jo, and M. Kim, "High-voltage-gain soft-switching converter employing bidirectional switch for fuel-cell vehicles," *IEEE Trans. Veh. Technol.*, vol. 70, no. 9, pp. 8731–8743, Sep. 2021.

Ji-Ho Choi (Graduate Student Member, IEEE) was born in Ulsan, Korea, in 1996. He received the B.S. degree in electronics and electrical engineering from Dongguk University, Seoul, South Korea, in 2021, where he is currently working toward the M.S. degree. His research interests include high efficient power circuit design, highly reliable hardware design, and grid-connected inverters and its control.

Muhammad Mubeen Khan received the B.S. and M.S. degrees in electrical engineering from University of Engineering and Technology, Taxila. He is currently working toward Ph.D. degree in electronics and electrical engineering with Dongguk University, Seoul, South Korea. His research interests include high efficient power circuit design, highly reliable hardware design, and grid-connected inverters and its control.

Cheol-Hwan Kim was born in Chungju, Korea, in 1997. He received the B.S. degree in electronics and electrical engineering from Dongguk University, Seoul, South Korea, in 2022, where he is currently working toward M.S. degree. His research interests include high efficient bidirectional converter design and its control.

Minsung Kim (Senior Member, IEEE) was born in Ulsan, Korea, in 1986. He received the B.S. degree in electrical engineering from Pohang University of Science and Technology (POSTECH), Pohang, South Korea, in 2008, and the Ph.D. degree in electrical engineering from POSTECH, Pohang, South Korea, in 2013. Since 2013, he has been with Department of Creative IT Engineering and Future IT Research Laboratory, POSTECH, Pohang, Korea, where he was a Research Assistant Professor. In 2016, he has worked as Research Scholar in Future Energy Electronics Center at Virginia Tech, Blacksburg, VA, USA. In 2017 and 2018, he has also served as an Academic Visitor in Control and Power System Group, Imperial College London, London, U.K. Since 2018, he has been with the Division of Electronics and Electrical Engineering, Dongguk University, Seoul, Korea, where he is currently an Associate Professor. His current research interests include highly efficient power conversion circuit design, intelligent controller design for industrial electronics, and renewable energy & energy storage systems.